33RD CONGRESS
OF THE INTERNATIONAL COUNCIL
OF THE AERONAUTICAL SCIENCES
STOCKHOLM, SWEDEN, 4-9 SEPTEMBER, 2022

ICAS 2022 SWEDEN

INVESTIGATION OF LEADING-EDGE VORTICES ON A TRIPLE-DELTA-WING CONFIGURATION USING SCALE-ADAPTIVE SIMULATION

Tony Di Fabbio[1], Eike Tangermann[1] & Markus Klein[1]

[1]University of the Bundeswehr Munich, Department of Aerospace Engineering, Institute of Applied Mathematics and Scientific Computing, 85577 Neubiberg, Germany, tony.difabbio@unibw.de

Abstract

A triple-delta wing configuration in transonic conditions has been investigated numerically with focus to the leading-edge vortices at sideslip flow. Two primary vortices occur in correspondence with the two wing sweep angles which interact with each other in the aft part of the wing. Besides, due to the transonic free-stream speed, several shock waves appear and also interact with the vortices. The side slip angle causes different flow conditions on the two wings, whose effects are connected. The present work focuses on the accuracy and efficiency of predicting aerodynamic coefficients and on analysis of the flow field to improve the understanding of the involved flow physical phenomena. Two different approaches of turbulence treatment have been applied and compared with the experimental data in order to determine the range of suitability of current turbulence models, namely scale-adaptive simulation (SAS) and kω-SST URANS. The SAS provides a promising approach to predict the flow physics over such configuration with a significantly better accuracy.

Keywords: Triple-delta wing, Leading-edge vortex, Vortex-vortex interaction, Scale-Adaptive Simulation

1. Introduction

Highly swept wings at extreme flight conditions feature complex flow fields which are challenging to predict. Such wings are typically found at agile military and supersonic aircraft since they provide suitable aerodynamic characteristics for flight at high Mach numbers. The high sweep angle permits for example to decrease the wave drag component during supersonic flight. The aerodynamic characteristics of the wing are dominated by a vortex system generated at the swept leading edge. For the design process of such aircraft, the detailed understanding and accurate prediction of this phenomenon is of primary importance.

A large amount of research has been carried out on aerodynamics of delta wings [1, 2]. In a wide variety of cases, reliable and realistic results can be achieved performing numerical simulations by applying RANS models with eddy viscosity based on the Boussinesq assumption that are very efficient in terms of computational time [3]. However, these eddy-viscosity turbulence models commonly are linear models derived from the Boussinesq hypothesis and they appear to lack capability to predict highly vortical flows. Therefore, they are not capable of predicting the flow sufficiently accurate in conditions of high angles of attack and side slip. The numerical simulations indeed often deviate from experimental data at higher angles of attack (AoA) especially in the vortex regions. For this reason, different approaches could be found in literature to overcome the deficiencies of the linear RANS approach [4, 5, 6]. No ultimate and general solution has, however, been found and several turbulence treatments need to be assessed in order to determine the range of their suitability for such specific and challenging wing configurations.

In the present work, the flow around the triple-delta wing ADS-NA2-W1 as described by [7] has been analysed not only to qualify turbulence model approaches but also to achieve a better understanding of the involved flow physics occurring over the aircraft at transonic conditions. The wing features a

sharp leading edge whereby the flow separation, which marks the initial stage of vortex formation, is fixed. For this reason, the main challenge within the simulation is to correctly produce formation and further development of the vortical flow system along the wing surface. Both the $k\omega$-SST URANS model and the scale-adaptive simulation (SAS) approach have been employed to explore their range of suitability. They primarily differ in terms of modeling or resolving turbulent fluctuations, which affects solution accuracy but also the required computational effort. The transonic regime of $Ma = 0.85$ and $Re = 12.53 \cdot 10^6$ with $\beta = 5°$ and $\alpha = 20°, 24°, 28°$ has been chosen, which features the phenomena of vortex-vortex interaction, vortex-shock interaction and vortex breakdown. The simulations have been performed employing the DLR TAU-Code [8].

In previous work by the authors [9, 10], promising improvements of accuracy have been achieved employing the SA-based hybrid RANS/LES approach. The results have shown great advancement in the prediction accuracy of the single and multiple-delta wing flow and revealed physical details of the vortex dynamics. However, despite the enormous effort required for the hybrid RANS/LES computations, some discrepancies between the numerical and the experimental results have been highlighted and explained which are suspected to be connected with grey-area effects and a slightly coarse mesh resolution in certain regions. The present work aims to improve the achieved results by applying the SAS model [11]. It allows for coarser mesh cells while still being well-defined at a higher degree of modeled turbulence. Further, the second model equation also can be beneficial especially in vortical flows.

The numerical results are validated using experimental data provided by Airbus Defence and Space [7]. Surface pressure coefficient and the aerodynamic coefficients demonstrate the effectiveness of the SAS approach. The focus is then set on the analysis of the vortex-vortex interaction phenomena between the two primary leading-edge vortices. Besides, the side slip angle provides different flow conditions on the two wings, whose effects are connected which will be discussed. Finally, an investigation on the vortex evolution focusing on the asymmetry of the turbulent flow under variation of the angle of attack is carried out.

2. Turbulence Modeling

The scale-adaptive simulation [11] is a method to allow the resolution of turbulence structures in unsteady flows. In this model, the von Kármán length scale is introduced into the scale determining equation which lets the model dynamically switch from RANS to LES-like behavior in unsteady regions of the flow field.

2.1 Scale-Adaptive Simulation equations

Currently, in the DLR TAU-Code solver the SAS is available based on the Menter $k\omega$-SST URANS model [12]. Within this model, the solution of the transport equations for turbulent kinetic energy k (Eq. 1) and dissipation rate ω (Eq. 2) yields the eddy viscosity.

$$\frac{\partial \rho k}{\partial t} + u_i \frac{\partial \rho k}{\partial x_i} = \tau_{ij} \frac{\partial u_i}{\partial x_j} - \beta^* \rho \omega k + \frac{\partial}{\partial x_j} \left[(\mu + \sigma_{k1} \mu_t) \frac{\partial k}{\partial x_j} \right] \tag{1}$$

$$\frac{\partial \rho \omega}{\partial t} + u_i \frac{\partial \rho \omega}{\partial x_i} = \frac{\gamma_1}{\nu_t} \tau_{ij} \frac{\partial u_i}{\partial x_j} - \beta_1 \rho \omega^2 + \frac{\partial}{\partial x_j} \left[(\mu + \sigma_{\omega 1} \mu_t) \frac{\partial \omega}{\partial x_j} \right] \tag{2}$$

To extend these governing equations to SAS capabilities, an additional source term Q_{SAS} is introduced in Eq. 2 for the turbulence eddy frequency.

$$Q_{SAS} = max \left[\rho \zeta_2 S^2 \left(\frac{L}{L_{vK}} \right)^2 - F_{SAS} \frac{2\rho k}{\sigma_\phi} max \left(\frac{1}{k^2} \frac{\partial k}{\partial x_j} \frac{\partial k}{\partial x_j}, \frac{1}{\omega^2} \frac{\partial \omega}{\partial x_j} \frac{\partial \omega}{\partial x_j} \right), 0 \right] \tag{3}$$

with the von Kármán length scale L_{vK} given by

$$L_{vK} = \kappa \frac{U'}{|U''|}; \quad U'' = \sqrt{\frac{\partial^2 U_i}{\partial x_k^2} \frac{\partial^2 U_i}{\partial x_j^2}}; \quad U' = \sqrt{2 \cdot S_{ij} S_{ij}} \tag{4}$$

and with the model constants

$$k = 0.41, \quad \zeta_2 = 1.755, \quad \sigma_\phi = 2/3, \quad F_{SAS} = 1.25 \tag{5}$$

2.2 Numerical Setup

The unsteady simulations have been performed with the DLR TAU-Code [8] using an implicit dual-time stepping approach and employing a Backward-Euler/LUSGS implicit smoother. Fluxes have been computed with a central scheme. In order to stabilize the URANS runs, an artificial dissipation of the central scheme has been added with the matrix dissipation method. In scale adaptive simulations the artificial dissipation has been reduced in order to prevent excessive damping of the resolved turbulent structures. A low-dissipation discretization scheme (LD) has therefore been used [8].

3. Triple-Delta-Wing Configuration

Fig. 1 shows the ADS-NA2-W1 geometry, which is a 1:30-scaled version of a generic combat aircraft. It is characterized by a triple-delta wing planform with three different leading-edge sections. More details about the wing configuration can be found in literature [7]. The dimensionless Cartesian coordinates are introduced as follows $\xi = x/L$, $\eta = y/(b/2)$, $\psi = z/(b/2)$.

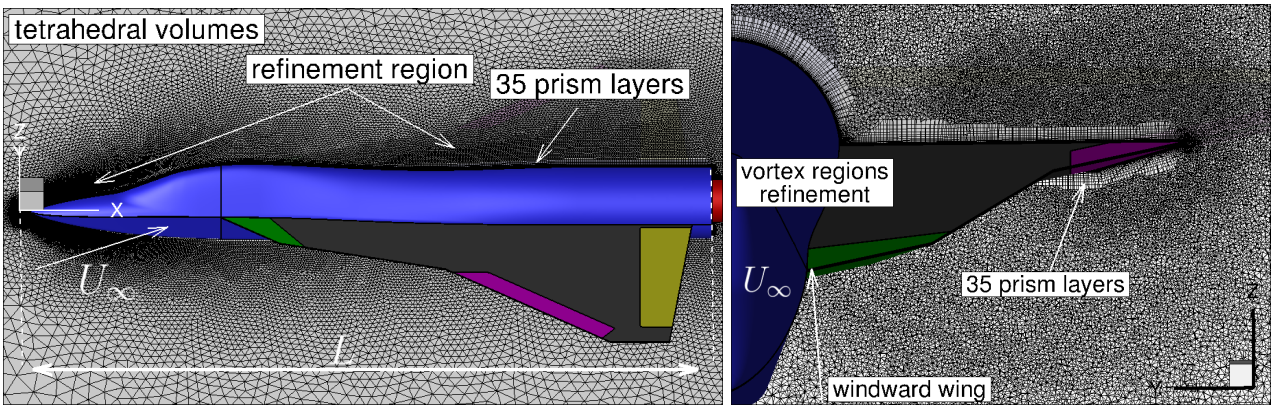

Figure 1 – ADS-NA2-W1 geometry and mesh

In previous work by the authors [9] the mesh has been validated in a convergence study. It has been performed with four different meshes, where the aerodynamic coefficients have been compared. For conciseness, the study is not included in the present manuscript.
The unstructured mesh employed to investigate the ADS-NA2-W1 geometry consists of about 40 million cells and it is formed by 35 prism layers close to the aircraft with the first cell layer thickness such that $y^+ \approx 1$ and tetrahedral volumes everywhere else. The domain size is 50 times the characteristic length L, which is the fuselage length. Figure 1 shows the inhomogeneous mesh, in which the cells size varies across the computational domain. The finest cells are located close to the leading edge where the two primary vortices are generated initially and the refinement roughly follows the vortices in order to capture their turbulent fluctuations.

4. Results

The flow features a Mach number of $Ma_\infty = 0.85$ and a Reynolds number of $Re_\infty = 12.53 \cdot 10^6$. URANS and SAS computations have been performed with constant side slip angle $\beta = 5°$, focusing on the asymmetry of the turbulent flow under varying angle of attack ($\alpha = 20°, 24°, 28°$).
The discussion of the results is structured as follows:

- In section 4.1 the lift, the rolling and the pitching moment coefficient curves are shown and compared with experimental data. Besides, the surface pressure coefficient is illustrated to analyse the evolution of the flow field over the aircraft. For further discussion the vortex center lines have been extracted from the SAS simulations at different angles of attack, which allows to illustrate flow properties of the vortex cores.

- The instantaneous flow features are visualized in section 4.2 to provide a comparison between the different SAS data for an understanding of vortex-vortex and vortex-shock interaction as well as vortex breakdown as the angle of attack increases. The focus is kept on changes to

the flow field by increased angle of attack. An interpretation of the vortex breakdown process is proposed and finally additional vortices are visualised.

4.1 Mean Flow Features

For a first overview of result accuracy achieved with the SAS approach, polar plots of the aerodynamic coefficients are included. They provide an overall impression of the surface pressure distribution and their accuracy is strongly affected by the correct prediction of the vortex systems. The flow physics is then described, explained and illustrated in detail by analysing the mean flow features.

4.1.1 Prediction of aerodynamic coefficients

Fig. 2 shows lift coefficient, pitching and rolling moment coefficient over angle of attack. Together with experimental data from [7], the SAnegRC URANS and DDES results discussed in the previous work [9] have been included as well for comparison with other model approaches. The curves show several steep changes which are caused by re-orientation of the vortices mostly associated with vortex breakdown. Due to the asymmetric flow, the vortex breakdown occurs at different angles of attack on windward and leeward side.

Since the integral moments react more sensitive to variations of the flow pattern than the force coefficients, the rolling and the pitching moment coefficient curves, plotted in Fig. 2b and 2c, respectively, are particularly relevant at non-zero side slip angle. The SAS results show a promising improvement of the aerodynamic coefficients even in comparison with the DDES results and overall it can be affirmed that the two equation $k\omega$ model is superior to the SA one equation model in the prediction of the flow field.

Recalling the analysis of the flow physics in [9], the significant deviation between the results of the different approaches at $\alpha = 20°$ is caused by the prediction of vortex breakdown on the windward wing. The vortex breakdown forms an abrupt change in the flow topology where the flow decelerates and diverges. This phenomenon is of high interest as it abruptly changes the aerodynamic characteristics of the aircraft. The still inaccurate prediction of the aerodynamic coefficients is mainly due to discrepancies between the measured and the simulated vortex breakdown onset position and strength or intensity, characterized by the rate of change of surface pressure, which both affect the suction footprint on the aircraft surface. Besides, at $\alpha \approx 27.5°$, the inboard vortex breaks down on the leeward wing and moves upstream from the trailing to the leading edge with increasing angle of attack. The lift reduction behind the vortex breakdown onset in the rear part of the leeward wing produces a nose-up (positive) pitching moment and a strong reduction of the rolling moment which even tends to negative values. As for the windward wing, the vortex breakdown on the leeward wing is predicted too far downstream by SAS still not producing a

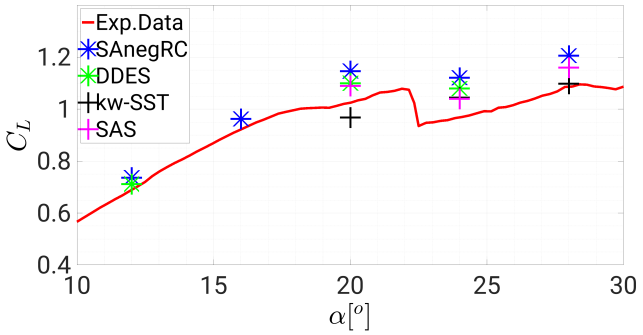

(a) Lift coefficient over AoA

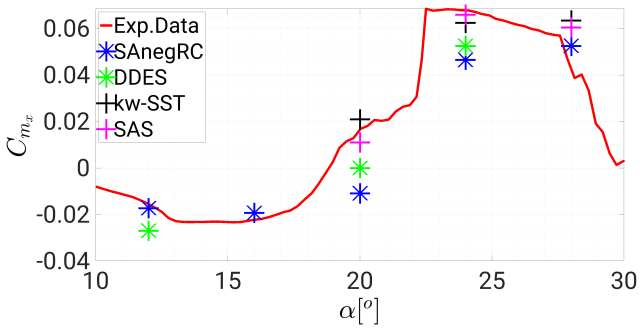

(b) Rolling moment coefficient over AoA

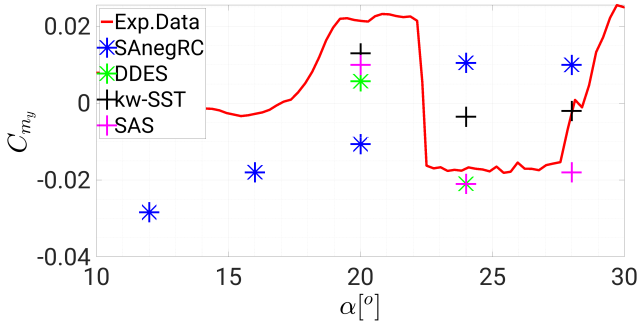

(c) Pitching moment coefficient over AoA

Figure 2 – Polar plots, comparison between experimental and numerical data with $Ma_\infty = 0.85$, $Re_\infty = 12.53 \cdot 10^6$ and $\beta = 5°$

sufficiently accurate prediction of the aerodynamic coefficients. However, as the SAS approach improves the agreement between experimental and numerical results, it is a promising tool to simulate the flow around the delta wing and it could certainly bring an advantage. A proper prediction of this phenomenon is of fundamental importance during the design and development phase of a delta wing aircraft.

4.1.2 Surface pressure

Fig. 3 shows the surface pressure coefficent on the aircraft from SAS at different angles of attack. Three different slice planes have been extracted and the distribution of the mean surface pressure coefficient $\overline{c_p}$ along the spanwise direction at chordwise positions $\xi = 0.35,\ 0.55,\ 0.75$ is then plotted in Fig. 4 comparing experimental data, $k\omega$-SST and SAS results. The numerical results have been assessed performing this comparison between all available data. Fig. 3 also shows indications of the vortex center lines (in black) that have been extracted using an automated criterion, which will be explained in sub-section 4.1.3.

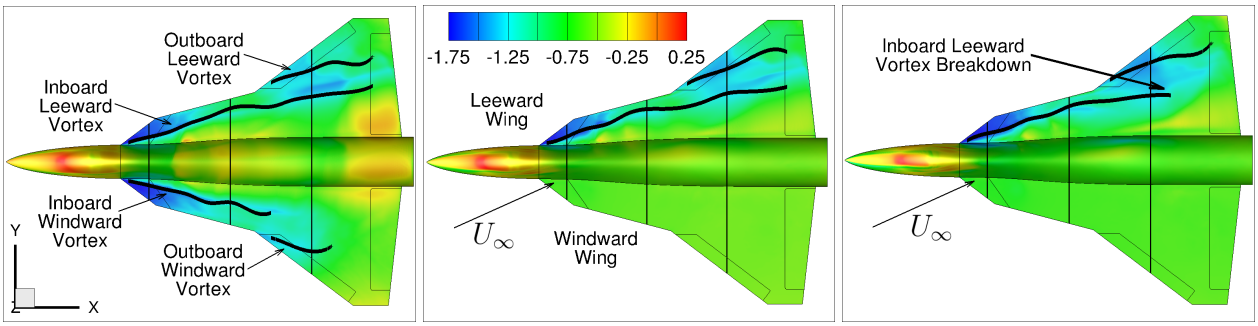

Figure 3 – Mean surface pressure coefficient $\overline{c_p}$, SAS results with $\alpha = 20°, 24°, 28°$ (from left to right). Black lines: vortex core lines.

As it can be seen in Fig. 4 from the surface pressure coefficient at the chordwise location $\xi = 0.35$, the SAS is able to capture the shear-layer separation and the primary vortex formation with a promising accuracy on both wings (windward and leeward) at lowest angle of attack. $k\omega$-SST results are also satisfactory, but SAS results are astounding, the numerical surface pressure coefficient matches the experimental one perfectly. The same accuracy is maintained on the leeward wing even at higher angles of attack.

The flow separates at the leading-edge and subsequently rolls up to form a stable, separation-induced primary vortex as will be discussed in section 4.2 The primary vortex then induces reattached flow over the wing, and under certain conditions the spanwise flow under the primary vortex subsequently separates a second time to form a counter-rotating secondary vortex outboard of the primary one. Only at mid-wing, the secondary vortex is well-structured and clearly visible. SAS captures the secondary vortex formation at the chordwise station $\xi = 0.55$, even though it is not as accurate as desired, since the negative pressure coefficient is overestimated ($\eta > 0.35$) at all angles of attack on the leeward wing.

At $\alpha = 20°$ and $24°$, the two fully developed primary vortices (inboard and outboard) are still distinguished on the leeward wing at the chordwise location $\xi = 0.75$ where the two peaks of $\overline{c_p}$ are located ($\eta > 0.5$), even though the two suction footprints are overestimated by the SAS. It is important to note that at $\alpha = 24°$ the inboard vortex is weaker and the outboard vortex stronger than the correspondents with $\alpha = 20°$. An exchange of energy between the vortices is suspected to be the reason. This mechanism of vortex-vortex interaction depends on the angle of attack. At the lower angle of attack ($\alpha = 20°$), the inboard vortex, which gains kinetic energy (the velocity inside the core rises), could be fed by the outboard one. This stabilizes the vortex which accelerates and remains stable. This does not work anymore at higher angles of attack, where this interaction loses power and the inboard vortex tends to break down in the aft part of the wing. Indeed, the breakdown on the leeward wing appears at $\alpha = 28°$, the $\overline{c_p}$ peak of the inboard vortex is not anymore present at chordwise location $\xi = 0.75$. The two vortices do not break down at the same location. Since the outboard vortex breaks

down after the inboard one, the $\overline{c_p}$ peak of the outboard vortex is still present at chordwise location $\xi = 0.75$ for $\eta \approx 0.6$.

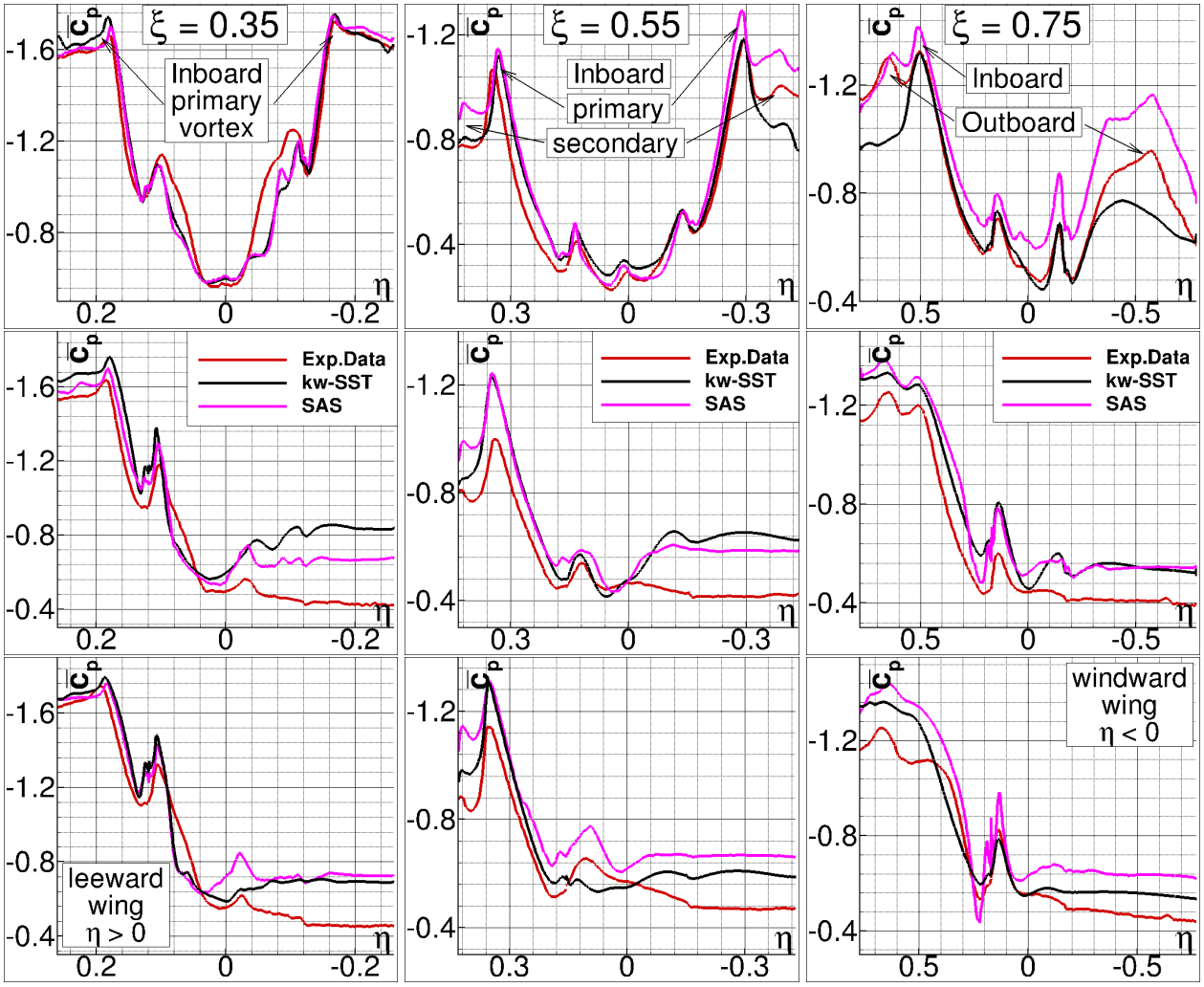

Figure 4 – Mean pressure coefficient $\overline{c_p}$ profiles at chordwise locations $\xi = 0.35,\ 0.55,\ 0.75$, comparison between experimental data, $k\omega$-SST URANS and SAS results with $\alpha = 20°$ (top), $24°$ (middle), $28°$ (bottom)

The situation is different on the windward wing. The results at $\alpha = 20°$ show that the vortices break down within the second half of the wing. The breakdown of the inboard vortex on the windward wing indeed can be visualized at chordwise location $\xi = 0.75$ in Fig. 4. In this case as well, they do not break down at the same location. The inboard vortex is the first to burst and subsequently the outboard vortex breaks down. The SAS model delays the prediction of breakdown, it is captured too far downstream on the wing compared to the experimental data. On the other hand, the $k\omega$-SST URANS results anticipate this phenomenon. This explains the slightly different predictions of the aerodynamic coefficients shown above in Fig. 2. The different prediction of the vortex breakdown onset is caused by the conditions upstream of the vortex. The secondary vortex formation needs to be considered in particular. As it can be seen on the windward wing at $\xi = 0.55$ for $\alpha = 20°$, the suction footprint generated by the primary inboard vortex on the windward wing is very similar (almost identical) in all results. The main discrepancies can be found in the secondary vortex. The captured $\overline{c_p}$ peak from the secondary vortex shows that the SAS result overestimates the strength of the secondary vortex with respect to experimental data. On the contrary, $k\omega$-SST URANS underestimates this phenomenon. In other words, the secondary vortex breaks down and prevents the shear-layer roll-up. The fluid forming the secondary vortex, which was rotating in opposite direction of the shear-layer, starts to fluctuate and forms a highly turbulent motion. From then on, this seemingly chaotic motion affects the shear-layer which thereby fails to roll up and feed the primary vortex. It is consequently

transported downstream along the wing causing the $\overline{c_p}$ profile visible at $\xi = 0.55$ for $\eta < -0.3$ in the $k\omega$-SST URANS results. This motion then influences the primary vortex, which loses its source of kinetic energy and becomes more vulnerable.
A similar behaviour that underlines this theory can be visualised on the leeward side at $\xi = 0.55$ for $\eta > 0.3$ in the $k\omega$-SST URANS results with $\alpha = 28°$. Here, as discussed above, the inboard burst vortex has been seen at chordwise location $\xi = 0.75$
Besides, as it can be evidenced by Fig. 2, the vortex breakdown onset moves upstream from the trailing to the leading edge with the increase of the angle of attack. At $\alpha = 24°$ the vortex breakdown on the windward wing has already reached the leading edge apex and remains fixed in that position, as the results at $\alpha = 28°$ confirm. Both $k\omega$-SST URANS and SAS capture the downstream transport of the shear layer over the windward wing at higher angles of attack even though the intensity of the suction footprint is slightly overestimated. Further, the difference between the numerical and the experimental suction footprint is almost constant and this constant gap could be related to the relatively high energy content of the unresolved scales of turbulence. However, a further refinement of the mesh appears unfeasible at present. The results confirm that the two equation model considerably improves the numerical results in comparison with the SA equation results discussed previously [9].

4.1.3 Vortex core line analysis on leeward wing

In order to investigate the flow field on the leeward wing more thoroughly, the vortex center lines have been extracted from the three different SAS simulations with $\alpha = 20°, 24°, 28°$. The resulting lines are shown in Fig. 5. The method considers the maximum of the mean swirl ($S = (\vec{\omega} \cdot \vec{u})/(\rho|\vec{u}|^2)$) in a delimited vortex region in order to determine the mean location of the vortex core over the wing. Fig. 5a shows that in the xy-plane the main difference is the behaviour of the outboard vortex. It is important to remember what emerged by analyzing the mean surface pressure coefficient: at $\alpha = 20°$ the inboard vortex is stronger and the outboard vortex weaker than the correspondents with $\alpha = 24°$. The results at $\alpha = 20°$ show that the outboard vortex moves first in the direction of the inboard one and they then tend towards the same trajectory. This is also the case where the two vortices are closer and therefore should interact more. Instead, at $\alpha = 24°$ the two vortices are much more separated but getting closer in the aft part of the wing. The interaction seems to be weaker and this confirms the previous considerations. The outboard vortex remains stronger and does not support the inboard one, which loses energy. The vortex-vortex interaction is not evident for $\alpha = 28°$ since the inboard vortex breaks down, as it is shown in Fig. 5a. The interaction process will be discussed deeper in section 4.2

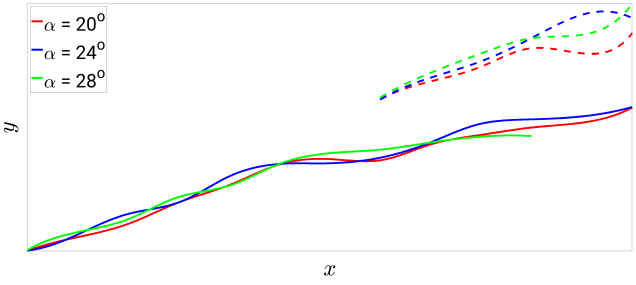

(a) xy-plane

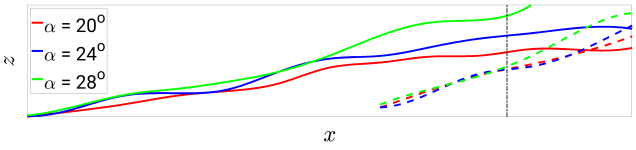

(b) xz-plane

Figure 5 – Leeward vortex core lines. SAS results with $\alpha = 20°, 24°, 28°$. Dashed lines indicate outboard, solid lines inboard vortex

It is also important to note how the vortex center lines evolve in the xz-plane while varying the angle of attack. From Fig. 5b it can be concluded that the vortices move upwards away from the wing as the angle of attack increases. The vortex inclination angle γ is measured from the data at the dashed black line in Fig. 5b. Fig. 6 shows then that a linear relationship exists between the angle of attack α and the vortex inclination angle γ with a slope of 0.5625. The three-dimensional nature of this phenomenon should be investigated in further work.
Fig. 7 shows the Mach number in the vortex core lines on the leeward wing, where the different locations of shock-vortex interaction can be identified as well. The shock-vortex interaction causes a reduction of the streamwise velocity and increases the vulnerability of the vortex [13]. The mean and instantaneous Mach number are plotted with solid and dashed lines in Fig. 7, respectively. Both quantities have been computed in the mean location of the vortex core.

The data has then been obtained from the mean and instantaneous flow field. Taking a look at the instantaneous lines, the vortex breakdown onset position seems to oscillate in a buffeting way and a clear onset point for the vortex breakdown cannot be determined.

The behaviour of the Mach number along the vortex cores is very similar for all the angles of attack. However, some important differences can be noted. First of all, the so-called trailing edge vortex [9] is located over the leeward wing only at $\alpha = 20°$. It is evinced at around $\xi = 0.85$ by the drop of the Mach, which is not present for the other angles of attack. Simulations at lower angles of attack are expected to show that the location of the trailing edge shock moves upstream over the wing as the angle of attack decreases. Further, the vortex speed close to the wing apex rises as expected at increasing angle of attack. However, especially at $\alpha = 28°$ a subsequent shock occurs, which causes a drop of the Mach number. Finally, as it can be then seen in Fig 7a at $\alpha = 28°$, the inboard windward vortex breaks down around $\xi = 0.7$ and meanwhile a shock wave is appears due to the abrupt changes in flow condition.

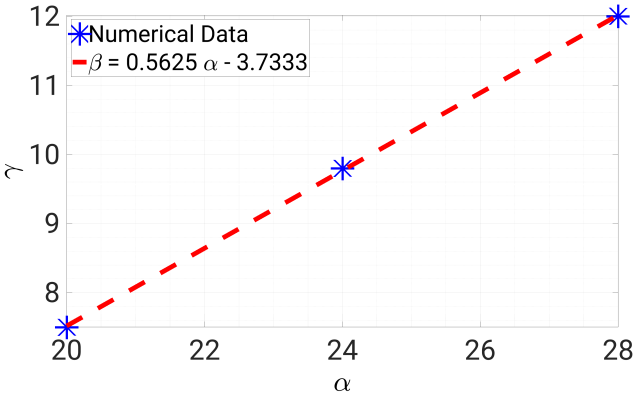

Figure 6 – Linear relationship between AoA and inboard vortex inclination angle. SAS results with $\alpha = 20°, 24°, 28°$

Fig. 7b shows the mean Mach number along the outboard leeward vortex core line. Regarding $\alpha = 28°$, a drop of $\overline{Ma}$ can be seen at around $\xi = 0.8$. It indicates the interaction between the inboard vortex breakdown and the outboard vortex. The outboard vortex consequently breaks then down around $\xi = 0.88$. The magnitude of the mean Mach number in the outboard vortex core in particular confirms that the aforementioned vortex is stronger at $\alpha = 24°$ than the correspondent with $\alpha = 20°$.

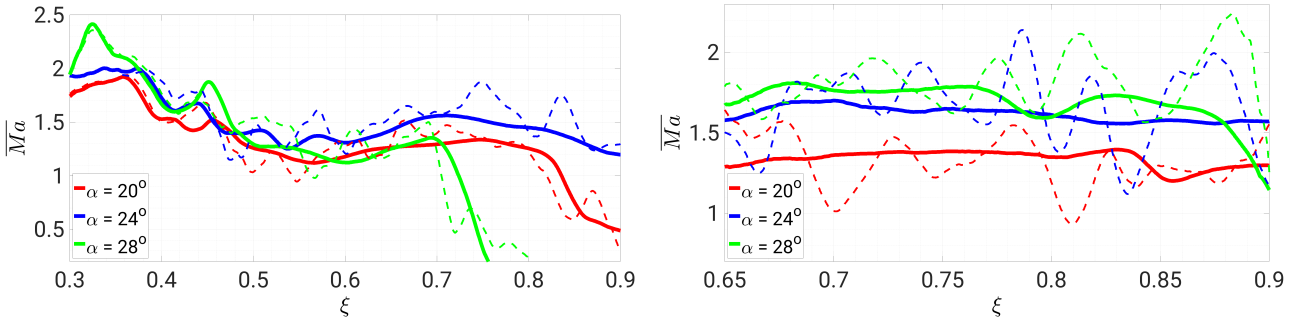

(a) Inboard leeward vortex

(b) Outboard leeward vortex

Figure 7 – Evolution of the Mach number $\overline{Ma}$ in the leading-edge vortex cores on the leeward wing. SAS results with $\alpha = 20°, 24°, 28°$. Dashed lines indicate instantaneous, solid lines averaged data.

4.2 Flow Evolution and Instantaneous Flow Features

Fig. 8 shows instantaneous flow fields from the SAS computations with $\alpha = 20°, 24°$ and $28°$. From both Q-criterion isosurfaces and streamlines it can be seen how the vortices are formed from the separated shear layer emanating from the leading-edge. The flow undergoes a primary separation over the wing passing the leading edge and subsequently rolls up to form a stable, separation-induced leading-edge vortex. On the left, Fig. 8 shows instantaneous surfaces from Q-criterion colored by Mach number and streamwise density gradient in red. The Q-criterion visualizes the vortices, whereas the density gradient highlights multiple shock waves over the aircraft. The interaction process between leading edge vortices and shock waves is crucial for understanding the flow physics at transonic conditions and has been addressed in detail in previous work [9, 10] including its effect on vortex breakdown. The following discussion will focus on the flow evolution by varying the angle of attack.

At $\alpha = 20°$, two well-distinguished vortices are present on the leeward wing and two less-distinguished

vortices are captured on the windward wing. The two vortices (inboard and outboard) are generated in correspondence with the two increasing sweep angles on the first and third leading edge sections. Both vortices on the windward wing then break down.

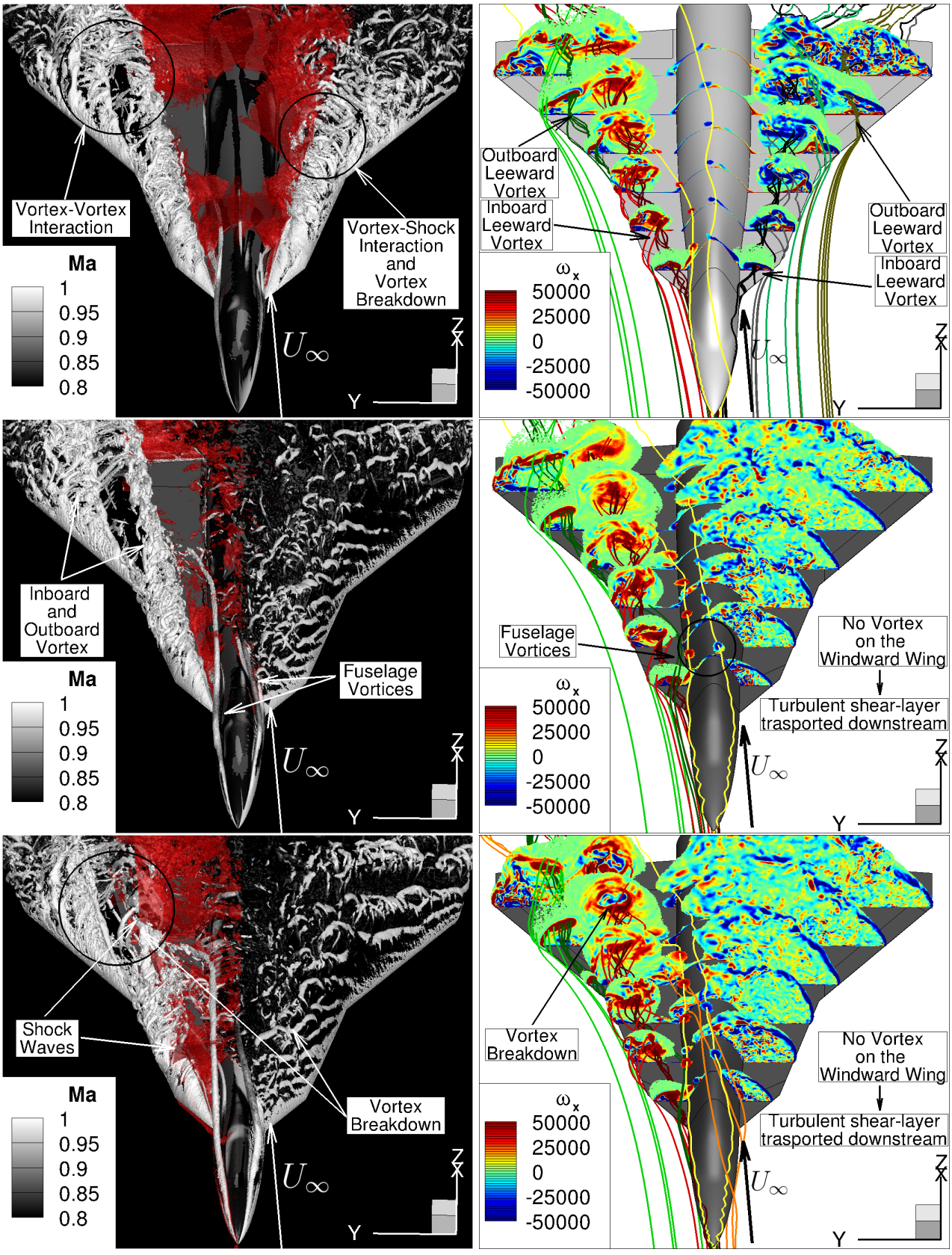

Figure 8 – Instantaneous iso-surfaces from Q-criterion colored by Mach number and streamwise density gradient in red (left), instantaneous streamwise vorticity and vortex stream-traces (right), SAS results for $\alpha = 20°$ (top), $24°$ (middle), $28°$ (bottom)

At $\alpha = 24°$, two coherent vortices are present on the leeward wing. The two vortices are less merged with each other compared to $\alpha = 20°$. As mentioned above, at lower angle of attack the inboard vortex gains kinetic energy (the velocity inside the core rises) because it is fed by the outboard one. The two vortices interact more with each other and follow the same trajectory, as Fig. 5 indicates. No coherent vortices are present on the windward wing. The flow becomes chaotic and turbulent, as the results in Fig. 8 show. In other words, the shear layer emanating from the leading edge is not rolling up to form a leading edge vortex over the wing any more, but is transported downstream without inducing additional velocities on the wing surface. An immediate consequence is the increase of the pressure over the wing and, consequently, the reduction of the suction footprint on the wing surface. By a rough and qualitative assessment of the resolution of turbulence in the turbulence-resolving areas, turbulent fluctuations are clearly visible in the trasported shear-layer or burst vortex and the level of resolution seems to be appropriate for an SAS computation, since even smaller turbulent structures appear to be resolved by the grid.
The same phenomenon is present on the windward wing for $\alpha = 28°$, because the vortex breakdown remains fixed at the wing apex once it reaches this location. The chaotic structures captured by SAS show how the burst vortex affects also the leeward wing in the aft part of the aircraft. This effect also increases with the angle of attack. Two leading-edge vortices are captured on the leeward wing which break down in the rear part of the wing interacting with a shock wave.
A mechanism behind the vortex breakdown occurrence has been proposed in sub-section 4.1.2 explaining the formation and breakdown of the secondary vortex by and below the inboard vortex. Fig. 8 shows that the shear-layer becomes more turbulent at increasing angle of attack which affects the formation and the stability of the secondary vortex. The onset of the inboard vortex is visualized in Fig. 8 from the vortex stream-traces shown together with instantaneous streamwise vorticity, which helps to distinguish the rotational direction between primary and secondary vortex. Streamlines of different colors are used to visualize several effects. The inboard vortex formation starts immediately downstream of the wing apex, the core of the inboard vortex is exclusively built from flow coming off the shear-layer that separates at the wing apex. The particles contained in the separated shear-layer emanating from the leading edge at the apex form the core of the inboard vortex and travel along the wing at very high speed as indicated by the black and bordeaux streamlines on the windward and leeward sides, respectively. The inboard vortex then grows in size because it is fed by the shear-layer all along the wing. This flow reinforces the main core by rotating around it and feeding it with kinetic energy. In this way the vortex is sustained, remains coherent and the axial velocity increases. The same mechanism can also be seen for the outboard vortex, whose core is mainly caused by the shear-layer separation at the second sweep angle increment. This leads to the conclusion that resolving separation and turbulence close to the wing apex is of primary importance for delta wing flow simulations.
As it has been commented in sub-section 4.1.3 , the mean location of the vortex changes as the angle of attack varies. It can be added to the discussion that the vortex shape depends on the angle of attack as well. The kidney shape expected at transonic conditions is more pronounced at higher angles of attack and this could be a sign of increased vulnerability of the vortex [14].
Finally, two more vortices are shown in Fig. 8 called fuselage vortices to distinguish them from leading-edge vortices. These vortices are generated from the flow passing the fuselage nose and they are located over the fuselage as indicated by the yellow stream-traces. They also depend on side slip angle and angle of attack being stronger and bigger at higher angle of attack. The fuselage vortices follow the direction of the free-stream flow and move towards the leeward wing affecting the flow on this wing. This considerably affects the flow between the fuselage and the leading-edge vortex as the leeward fuselage vortex is finally merged into the inboard leading edge vortex.

5. Conclusion and Outlook

Both $k\omega$-SST URANS and Scale-Adaptive Simulation (SAS) have been employed in order to investigate the vortex-dominated flow around the generic triple-delta wing aircraft ADS-NA2-W1. Transonic flow conditions with $M_\infty = 0.85$ and $Re_\infty = 12.53 \cdot 10^6$ have been selected. Different simulations have been performed at varying angle of attack ($\alpha = 20°, 24°, 28°$) with constant side slip angle $\beta = 5°$.

Within the scope of this work, a better understanding of several flow physical phenomena over the aircraft has been achieved and the range of suitability of current CFD methods has been extended. The flow field has been illustrated and discussed in detail divided into the analysis of mean flow features (sub-section 4.1), which comprise aerodynamic coefficients, surface pressure coefficient and the vortex core line analysis, and unsteady (instantaneous) flow features (sub-section 4.2).
Promising improvements compared to previous results have been achieved employing two equation closure models. Both approaches improve the prediction of the aerodynamic coefficients, as it has been discussed in sub-section 4.1.1. The accuracy of the integral moment coefficients (pitching and rolling) is mainly related with the prediction of vortex breakdown. It affects the suction footprint over the wings and consequently the surface pressure coefficient downstream of the vortex breakdown. The vortex breakdown phenomenon is of high interest as it abruptly changes the aerodynamic characteristics of a delta wing. Its proper prediction is of fundamental importance during the design and development phase of a delta wing based aircraft. The vortex flow pattern has been investigated in detail leading to the explanation of a mechanism connected with vortex breakdown.
SAS is a promising tool to simulate the flow physics around a delta wing. It might serve as a reference model for such test cases, even at more challenging conditions and configurations. It is capable of producing a similar accuracy as hybrid RANS/LES but at significantly reduced computational effort. In the present case, SAS provides a reduction of computing time by 37% compared to DDES. In continuation of this analysis, further steps will focus on analysis of other specific features, such as identifying the attachment and separation lines, or switching to a vortex-fitted coordinate system. Also the unsteady nature of the flow will be investigated in terms of rotational frequencies as well as shock buffeting. Finally, turbulence-related variables such as components of the Reynolds stress tensor and length scales need to be assessed in detail to better understand the turbulent flow field.

Acknowledgment

Funding of this investigation by Airbus Defence and Space within the project "Efficient Turbulence Modelling for Vortical Flows from Swept Leading Edges" is gratefully acknowledged as well as the support with experimental data of the ADS-NA2-W1 aircraft. The authors gratefully acknowledge the German Aerospace Center (DLR) for providing the DLR TAU-Code used for the numerical investigation of the present research. Furthermore, providing the meshing software by Ennova Technologies Inc. is sincerely appreciated. The authors thank to the Gauss Centre for Supercomputing for funding this project by providing computing time on the GCS Supercomputer SuperMUC at Leibniz Supercomputing Center (account number pn29xa).

Contact Author Email Address

To facilitate future contacts and ask any questions mailto: tony.difabbio@unibw.de

Copyright Statement

References

[1] R. Konrath, C. Klein, and A. Schröder, “PSP and PIV investigations on the VFE-2 configuration in sub- and transonic flow,” (Reno, Nevada), 46th AIAA Aerospace Sciences Meeting and Exhibit, 2008.

[2] E. Tangermann, A. Furman, and C. Breitsamter, “Detached eddy simulation compared with wind tunnel results of a delta wing with sharp leading edge and vortex breakdown,” (New Orleans, Louisiana), 30th AIAA Applied Aerodynamics Conference, 2012.

[3] M. Werner, A. Schütte, and S. Weiss, “Turbulence model effects on the prediction of transonic vortex interaction on a multi-swept delta wing,” (San Diego, CA), AIAA SCITECH Forum, 2022.

[4] M. Moioli, C. Breitsamter, and K. Sørensen, “Turbulence modeling for leading-edge vortices: an enhancement based on experimental data,” (Orlando, FL), AIAA SciTech Forum, 2020.

[5] P. R. Spalart, "Strategies for turbulence modelling and simulations," *International Journal of Heat and Fluid Flow*, vol. 21, no. 3, pp. 252–263, 2000.

[6] C. L. Rumsey, J.-R. Carlson, T. H. Pulliam, and P. R. Spalart, "Improvements to the quadratic constitutive relation based on nasa juncture flow data," *AIAAJ*, vol. 58, 2020.

[7] A. Hövelmann, A. Winkler, S. M. Hitzel, K. Richter, and M. Werner, "Analysis of vortex flow phenomena on generic delta wing planforms at transonic speeds," in *New Results in Numerical and Experimental Fluid Mechanics XII*, (Cham), pp. 307–316, Springer International Publishing, 2020.

[8] A. Probst and S. Reuß, "Progress in scale-resolving simulations with the dlr-tau code," (Braunschweig, Deutschland), Deutscher Luft- und Raumfahrtkongress, 2016.

[9] T. Di Fabbio, E. Tangermann, and M. Klein, "Investigation of transonic aerodynamics on a triple-delta wing in side slip conditions," *CEAS Aeronautical Journal*, Feb 2022.

[10] T. Di Fabbio, E. Tangermann, and M. Klein, "Flow pattern analysis on a delta wing at transonic speed," (San Diego, CA), AIAA SCITECH 2022 Forum, 2022.

[11] F. R. Menter and Y. Egorov, "The scale-adaptive simulation method for unsteady turbulent flow predictions. part 1: Theory and model description," *Flow, Turbulence and Combustion*, vol. 85, pp. 113–138, Jul 2010.

[12] F. R. Menter, "Two-equation eddy-viscosity turbulence models for engineering applications," *AIAA Journal*, vol. 32, no. 8, p. 1598–1605, 1994.

[13] J. M. Delery, "Aspects of vortex breakdown," *Progress in Aerospace Sciences*, vol. 30, no. 1, p. 1–59, 1994.

[14] J. Riou, E. Garnier, and C. Basdevant, "Compressibility effects on the vortical flow over a 65° sweep delta wing," *Physics of Fluids*, no. 3, pp. 35–102, 2010.